

## The Role of Ligand Packing Frustration in Body-Centered Cubic (bcc) Superlattices of Colloidal Nanocrystals

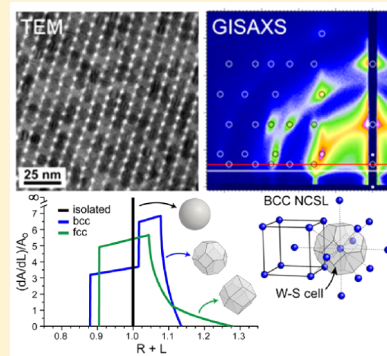
Brian W. Goodfellow,<sup>†</sup> Yixuan Yu,<sup>†</sup> Christian A. Bosoy,<sup>†</sup> Detlef-M. Smilgies,<sup>‡</sup> and Brian A. Korgel\*,<sup>†</sup>

<sup>†</sup> McKetta Department of Chemical Engineering, Texas Materials Institute, Center for Nano and Molecular Science and Technology, The University of Texas at Austin, Austin, Texas 78712-1062, United States

<sup>‡</sup> Cornell High Energy Synchrotron Source (CHESS), Cornell University, Ithaca, New York 14853, United States

### Supporting Information

**ABSTRACT:** This paper addresses the assembly of body centered-cubic (bcc) superlattices of organic ligand-coated nanocrystals. First, examples of bcc superlattices of dodecanethiol-capped Au nanocrystals and oleic acid-capped PbS and PbSe nanocrystals are presented and examined by transmission electron microscopy (TEM) and grazing incidence small-angle X-ray scattering (GISAXS). These superlattices tend to orient on their densest (110) superlattice planes and exhibit a significant amount of {112} twinning. The same nanocrystals deposit as monolayers with hexagonal packing, and these thin films can coexist with thicker bcc superlattice layers, even though there is no hexagonal plane in a bcc lattice. Both the preference of bcc in bulk films over the denser face-centered cubic (fcc) superlattice structure and the transition to hexagonal monolayers can be rationalized in terms of packing frustration of the ligands. A model is presented to calculate the difference in entropy associated with capping ligand packing frustration in bcc and fcc superlattices.



This paper concerns the self-assembly of ligand-coated nanocrystals into body-centered cubic (bcc) superlattices and examines the role of ligand packing frustration as a key driving force that determines such assembly. Underlying this issue is the fact that dense collections of *hard sphere* particles order into close-packed face-centered cubic (fcc) lattices—not bcc—to maximize free volume entropy.<sup>1–4</sup> Sterically stabilized, uniform colloidal nanocrystals—with their relatively short-range repulsive interactions—also form fcc superlattices.<sup>5–10</sup> However, bcc superlattices of nanocrystals are also quite common, and nanocrystals with the same chemical makeup can form both structures.<sup>11–25</sup> This superlattice structure polymorphism was first observed in alkanethiol-coated Au<sup>12,14,20</sup> and Ag<sup>11,19</sup> nanocrystals made with different ratios of ligand length to core radius,  $\langle L \rangle / R$ . When  $\langle L \rangle / R$  was greater than 0.6–0.7, bcc superlattices were favored. This shift from fcc to bcc order with increasing interparticle separation is qualitatively similar to what happens in concentrated dispersions of charge-stabilized colloidal particles and polymer micelles.<sup>26–29</sup> The fcc–bcc superlattice transition for ligand-coated nanocrystals has been interpreted using a statistical mechanical analysis using empirical nanocrystal pair interaction potentials and correlation functions,<sup>3</sup> molecular dynamics simulations of ligand-capped nanocrystals,<sup>30</sup> geometric calculations of ligand space-filling,<sup>31</sup> and simulations of faceted nanocrystals with variations in ligand coating uniformity.<sup>15,16,25</sup> We have suggested that the conformational entropy of the capping ligands can also be important,<sup>32</sup> and explain, for example, the observed coexistence of thick bcc superlattice films with hexagonal monolayers of the same nanocrystals, even though there is no close-packed plane

in a bcc lattice.<sup>13</sup> This is analogous to sphere-forming amphiphilic diblock copolymers, which preferentially order with bcc structure in bulk films,<sup>33–37</sup> and also form hexagonal monolayers when deposited as thin films.<sup>35,38</sup>

Essentially, there is an entropic penalty induced by superlattice formation that arises from ligand packing constraints.<sup>32,36–38</sup> The ligands prefer to uniformly extend from the nanocrystal surface, yet the space-filling constraints in the superlattice do not allow this. Here, we provide a model to calculate and compare the entropic penalty for ligand packing frustration in fcc and bcc superlattices, and show why ligand packing frustration always favors bcc structure. When  $\langle L \rangle / R$  is relatively large and the van der Waals attraction between inorganic cores is largely screened by the repulsive interactions of the ligand shells,<sup>39,40</sup> this entropic penalty becomes significant. The model also reveals that the relative contributions due to ligand compression and extension from equilibrium chain length are different for bcc and fcc lattices and ligand interpenetration within the superlattices further favors bcc structure.

Figure 1 shows grazing incidence small-angle X-ray scattering (GISAXS) and transmission electron microscopy (TEM) data obtained from bcc superlattices of dodecanethiol-capped Au (1.8 nm diameter), oleic acid-capped PbS (3.7 nm diameter), and oleic-acid capped PbSe (7.9 nm diameter) nanocrystals. The nanocrystal syntheses are described in the Supporting

Received: May 7, 2015

Accepted: June 8, 2015

Published: June 8, 2015



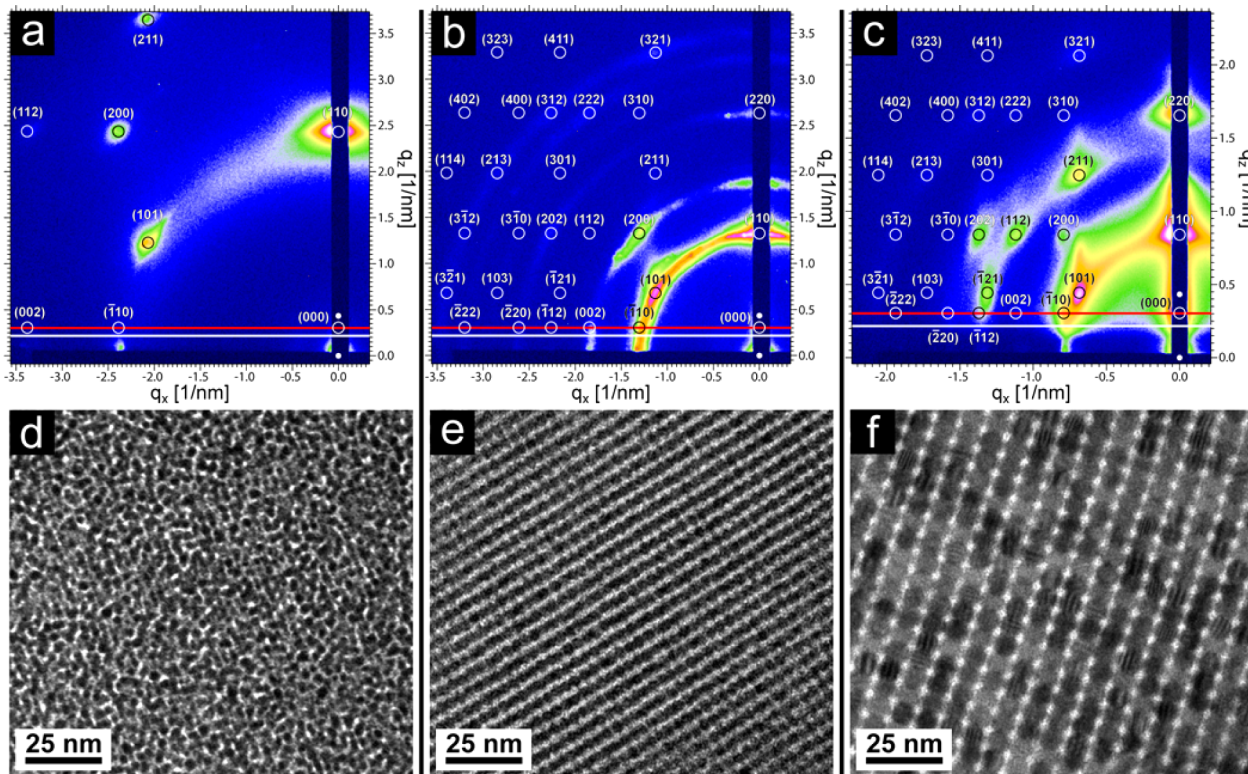


**Figure 1.** (a–c) GISAXS patterns and (d–f) TEM images of bcc superlattices of (a,d) 1.8 nm diameter dodecanethiol-capped Au nanocrystals, (b,e) 3.7 nm diameter oleic acid-capped PbS nanocrystals, and (c,f) 7.9 nm diameter oleic acid-capped PbSe nanocrystals. The spot indexing (open circles) of the GISAXS patterns corresponds to a (110) oriented bcc superlattice with a lattice constant,  $a_{\text{bcc}}$ , of (a) 3.72 nm, (b) 6.80 nm, and (c) 11.2 nm. The solid white dots indicate the direct and reflected X-ray beam positions and the horizontal lines indicate the sample horizon (white) and the Yoneda peak for the film (red).<sup>41</sup>

**Table 1. Summary of Nanocrystal Size and Superlattice Parameters**

core material	capping ligand	core radius <sup>a</sup> ( $R$ ; nm)	bcc superlattice constant <sup>b</sup> ( $a_{\text{bcc}}$ ; nm)	nearest-neighbor spacing <sup>c</sup> ( $r_{\text{NN}}$ ; nm)	characteristic ligand length <sup>d</sup> ( $L_o$ ; nm)
Au	dodecanethiol	0.90	3.72	3.22	0.93
PbS	oleic acid	1.85	6.80	5.89	1.50
PbSe	oleic acid	3.95	11.20	9.70	1.56

<sup>a</sup>Determined from solution SAXS (see Supporting Information). <sup>b</sup>Determined from GISAXS. <sup>c</sup> $r_{\text{NN}} = a_{\text{bcc}} \sqrt{3}/2$ . <sup>d</sup> $L_o = a_{\text{bcc}}(3/8\pi)^{1/3} - R$ .

Information. All of these superlattices are oriented with (110) superlattice planes on the substrate. The (110) plane has the highest planar packing density in the bcc lattice, similar to the (111) plane of an fcc lattice with a slight in-plane distortion. The radius of the inorganic nanocrystal cores  $R$ , was measured by solution SAXS (see Supporting Information) and the superlattice lattice constants  $a_{\text{bcc}}$  were determined from GISAXS. These values were used to calculate the nearest neighbor spacing ( $r_{\text{NN}}$ ) and characteristic ligand lengths ( $L_o$ ) in the superlattices, which are summarized in Table 1. These nanocrystals, with three different core compositions have a range of  $\langle L \rangle/R$  values, further showing that bcc superlattice formation is a rather general occurrence. For the bcc superlattices shown in Figure 1, the values of  $\langle L \rangle = 0.12(m + 1)$  ( $m$  is the number of carbon atoms) are 1.56 nm for dodecanethiol and 2.28 nm for oleic acid, and  $\langle L \rangle/R$  is 1.73 for the Au nanocrystals, 1.23 for the PbS nanocrystals and 0.58 for the PbSe nanocrystals.

To understand how capping ligand packing frustration can influence superlattice structure, it is first necessary to consider that the capping ligands are like identical springs and prefer to

distribute with uniform extension around the inorganic nanocrystal core. This spherically symmetric arrangement of hydrocarbon chains can exist when the nanocrystals are freely dispersed in a solvent, but not in a superlattice. In a superlattice, the ligand shells must conform to the volume available in the space-filling polyhedra, or Wigner–Seitz (W–S) cells, as shown in Figure 2. This forces the ligands to either stretch or compress from their equilibrium length. The bcc W–S cell is more spherically symmetric than the fcc W–S cell and therefore allows a more uniform ligand shell thickness and places less of an entropic penalty on the ligand distribution. This is precisely the reason that sphere-forming amphiphilic diblock copolymers prefer to form bcc structures over fcc.<sup>36</sup>

The difference in ligand conformational entropy for fcc and bcc superlattices can be estimated from the ligand length distribution around the nanocrystals within the W–S cell. Figure 3 shows the ligand length distribution plotted as a normalized probability density that an element of the W–S cell surface area is at a distance,  $R + L$ , from the center of the nanocrystal.  $L$  is the distance to the boundary of the W–S cell. The average ligand length—or in other words, the average

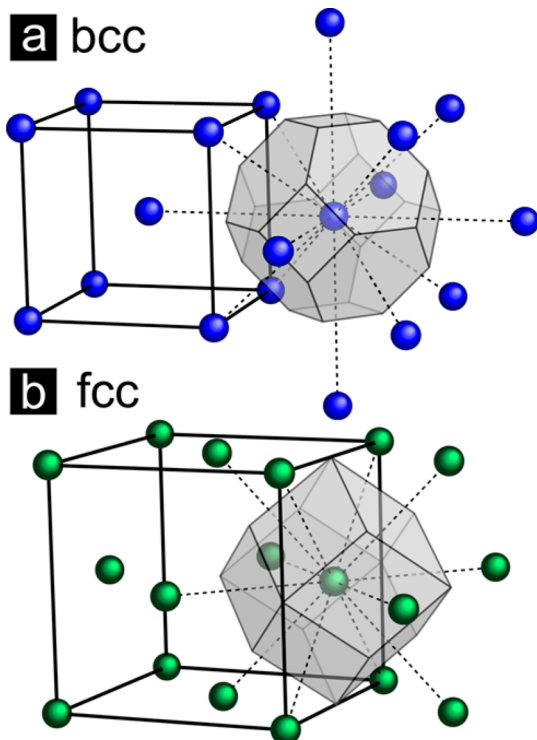


**Figure 2.** Unit cells and Wigner–Seitz (W–S) cells for (a) bcc and (b) fcc lattices. The bcc and fcc W–S cells are truncated octahedra and rhombic dodecahedra, respectively. The bcc W–S cell is more spherically symmetric than the fcc W–S cell. The sphericities of the bcc and fcc W–S cells are 0.9099 and 0.9047. The sphericity of a sphere is one.

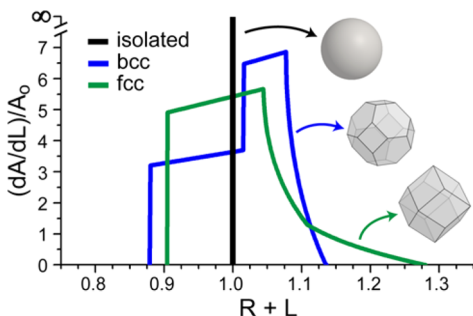


**Figure 3.** Plot of the normalized probability density ( $[dA/dL]/A_o$ ) that an element of the W–S cell surface exists at a distance,  $R + L$ , from the center of the W–S cell. The total surface area of the W–S cell is denoted by  $A_o$ . The volume of each W–S cell is normalized so that the W–S radius,  $R_s = R + L_o = 1$ . To quantify the difference in anisotropy of the W–S cell, the standard deviations in the distribution of ligand lengths were determined. They are  $0.063(R + L_o)$  and  $0.070(R + L_o)$  for the bcc and fcc superlattices, respectively, or in other words, 11% greater for the fcc superlattice. Calculation details are provided in the Supporting Information.

ligand shell thickness—is  $L_o$ . This is the equilibrium capping ligand length for an isolated nanocrystal and the chain length that maximizes the number of ligand conformations. In the superlattice, the ligand shells deviate from  $L_o$  by stretching and compressing to fill the volume of the W–S cell. From Figure 3 it is apparent that the ligand shells exhibit more significant compression in the bcc superlattice and more significant extension in the fcc superlattice.

The conformational entropy of a single ligand molecule is calculated using a freely jointed chain model:

$$S(L) = k_B \ln(P(L)) \quad (1)$$

where  $k_B$  is Boltzmann's constant and  $P(L)$  is the relative number of ligand conformations for a ligand of length  $L$ ,

$$P(L) = 4\pi \left( \frac{1}{L_o \sqrt{\pi}} \right)^3 L^2 \exp\left(-\frac{L^2}{L_o^2}\right) \quad (2)$$

The volume occupied per nanocrystal,  $\nu_s = 1/\rho$ , is the volume of the W–S cell and is determined from the superlattice parameter determined by GISAXS:

$$\nu_s = \frac{1}{\rho_n} = \frac{a_{bcc}^3}{2} = \frac{a_{fcc}^3}{4} \quad (3)$$

The characteristic radius  $R_s$  of the W–S cell in the superlattice is

$$R_s = \left( \frac{3\nu_s}{4\pi} \right)^{1/3} \quad (4)$$

The characteristic ligand length in the superlattice  $L_o$  is then  $L_o = R_s - R$ , where  $R$  is the radius of the nanocrystal core:

$$L_o = a_{bcc} \left( \frac{3}{8\pi} \right)^{1/3} - R = a_{fcc} \left( \frac{3}{16\pi} \right)^{1/3} - R \quad (5)$$

Table 1 lists the values of  $R$ ,  $a_{bcc}$ , and  $L_o$  determined experimentally by SAXS and GISAXS for the superlattices examined in Figure 1. Both values of  $L_o$ , of 0.93 nm for dodecanethiol and 1.53 nm (average value) for oleic acid capping ligands, are significantly smaller than the fully extended chain lengths of 1.56 and 2.28 nm because of the significant interstitial volume filled by the ligands between the inorganic cores in the superlattice.<sup>6</sup>

The total entropy of the organic ligand shell  $S_{\text{lig}}$  is then computed by summing the entropy of all of the ligands on the nanocrystal:

$$S_{\text{lig}} = \sum_L S(L)n(L) \quad (6)$$

where  $n(L)$  is the number of chains with length  $L$ . The conformational entropy of the ligands is then compared for bcc and fcc superlattices by maintaining the same volume of the bounding cells  $V$ , and number of ligands in the capping layer  $N$ .  $N$  depends on  $R$ , the packing fraction of ligands on the nanocrystal surface  $\phi_s$ , and the areal footprint of the ligand on the nanocrystal surface  $A_{\text{lig}}$ :

$$N = \frac{4\pi R^2 \phi_s}{A_{\text{lig}}} \quad (7)$$

For a free or isolated nanocrystal, all of the ligands are at their equilibrium length  $L_o$ , so that

$$S_{\text{lig,iso}} = S(L_o)N \quad (8)$$

The distributions of the ligand length in the W–S cell (as shown in Figure 3) are then used to determine the conformational entropy of the capping ligand layer in the bcc and fcc superlattices,  $S_{\text{lig,NCSL}}$ . The change in conformational entropy of the ligand shell  $\Delta S_{\text{lig}}$  occurring upon superlattice assembly is then

$$\Delta S_{\text{lig}} = \frac{N_A}{N} (S_{\text{lig,NCSL}} - S_{\text{lig,iso}}) \quad (9)$$

where  $N_A$  is Avogadro's number.

Values of  $\Delta S_{\text{lig}}$  are shown in Figure 4. Superlattice assembly frustrates the ligand packing entropy in both bcc and fcc

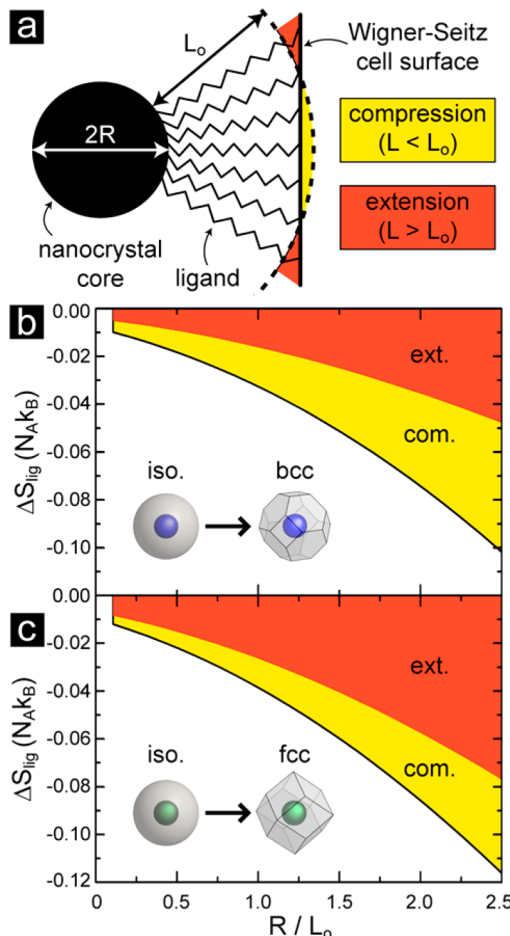


**Figure 4.** (a) Illustration of a nanocrystal with inorganic core of radius  $R$ , coated with capping ligands spanning a distribution of lengths  $L$ , from the nanocrystal core to the surface of the W–S cell. The ligand shells must be extended and compressed from their equilibrium thickness  $L_o$  to fill the W–S cell. The difference in the ligand conformational entropy of isolated (iso.) nanocrystals and those ordered into (b) bcc and (c) fcc superlattices,  $\Delta S_{\text{lig}}$ , is plotted as a function of  $R/L_o$ .  $\Delta S_{\text{lig}}$  is calculated per mole of ligands in units of the gas constant ( $N_A k_B$ ). The contributions to  $\Delta S_{\text{lig}}$  due to compressed (comp.) and extended (ext.) ligands have been shaded yellow and red, respectively. Ligand interpenetration between neighboring W–S cells eliminates the compressive contribution to  $\Delta S_{\text{lig}}$ .

superlattices, but the entropic penalty is slightly larger in fcc. The entropic penalty to form an fcc superlattice is about 15% greater than the bcc superlattice.  $\Delta S_{\text{lig}}$  also increases with increasing particle size. This is simply due to the greater number of ligands coating the surface of larger nanocrystals. This does not mean that larger nanocrystals will have a higher tendency to form bcc superlattices, as the van der Waals attraction between the inorganic cores becomes much stronger for the larger nanocrystals, and these cohesive attractions always strongly favor fcc.<sup>11</sup> The packing ligand frustration is only expected to be important when the core size is small

relative to the chain length and interparticle attractions become weak.<sup>39</sup>

Figure 4 also shows the relative contributions of ligand shell compression and extension to  $\Delta S_{\text{lig}}$  for bcc and fcc superlattices. As the ligand length distribution in Figure 3 shows, the ligand shell exhibits greater compression in the bcc superlattice, and greater extension in the fcc superlattice. Some interpenetration of ligand chains is expected.<sup>25,34</sup> If ligands can interpenetrate between neighboring W–S cells, some of the compression in the ligand shell could be relieved. In other words, the “compressed” ligands with  $L < L_o$  that would give rise to the entropic contribution shaded in yellow in Figure 4b,c, can relax in the W–S cell toward  $L_o$  when interpenetration is allowed; thus, reducing the contribution to  $\Delta S_{\text{lig}}$  from the compressed ligands. In that case, the entropy penalty would result predominantly from the extended ligands, which is significantly greater in the fcc superlattices than in bcc—by about 60%. The likelihood of chain interpenetration furthermore becomes greater when  $\langle L \rangle / R$  increases, as a result of the higher surface curvature and increased free volume between capping ligands further from the nanocrystal surface.<sup>42</sup> In the case of lead chalcogenide nanocrystals, the double bond in oleic acid leads to lower ligand packing density than alkyl-based ligands, not to mention that surface oxidation of PbS and PbSe can easily lead to ligand desorption, resulting in the possibility of more ligand interpenetration compared to alkanethiol-capped metal nanocrystals at similar  $\langle L \rangle / R$  values.<sup>13,15,16,25</sup>

Ligand packing frustration also explains the observed coexistence of thick bcc superlattice films and hexagonal monolayers made from the same nanocrystals,<sup>13</sup> even though there is no close-packed plane in a bcc lattice. Figure 5 shows a TEM image of such a structural transition for PbSe nanocrystals. The nanocrystals in the thicker region exhibit bcc superlattice structure, while the monolayer is hexagonally close-packed. Such a structural transition is also well-known for thin films of sphere-forming amphiphilic diblock copolymers.<sup>35,38</sup> This is also a result of chain packing frustration. As shown in Figure 5, the 2D W–S cells of a hexagonal monolayer are more rotationally symmetric than the 2D W–S cells of a bcc (110) plane, thus eliminating some ligand packing frustration.

We also observe high concentrations of twinned grain boundaries in the bcc superlattices. Figure 6 shows some examples of twins in bcc PbS and PbSe nanocrystal superlattices. Others have observed twinning in bcc superlattices of Au nanocrystals<sup>20</sup> and bcc AB<sub>6</sub> binary superlattices of Au and Fe<sub>3</sub>O<sub>4</sub> nanocrystals.<sup>43</sup> Twinning occurs on {112} crystal planes of the superlattice, which are the expected twin plane for a bcc crystal. {112} twin defects are also commonly observed in bcc assemblies of polymer micelles<sup>44</sup> and larger colloidal particles.<sup>45</sup> Twinning is not usually reported for fcc superlattices, although it has been observed in large single-crystals of fcc superlattice of Au nanocrystals.<sup>46</sup> One difference between fcc and bcc superlattice twins is their relative orientation with respect to the substrate. Twinning in an fcc crystal occurs on {111} crystal planes, and since nanocrystal superlattices tend to deposit with the highest density plane oriented on the substrate, i.e., (111) for fcc and (110) for bcc, the {111} twins in an fcc superlattice can be oriented perpendicular to the observation angle in the TEM, making it impossible to see them. Other (111) twin plane orientations would require a 19.47° tilt angle to image down the twin plane. On the other

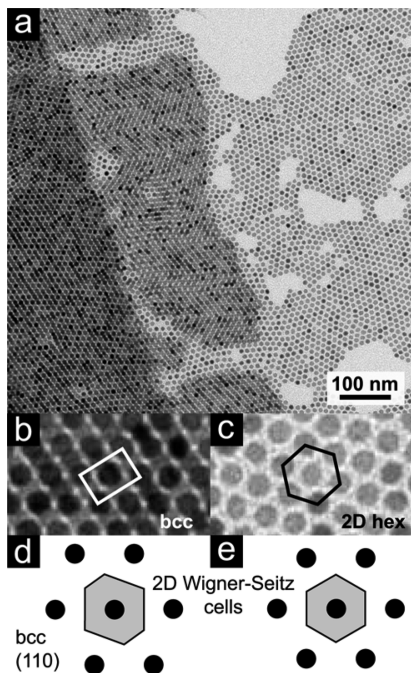


**Figure 5.** (a) TEM image of 9.5 nm diameter oleic acid-capped PbSe nanocrystals exhibiting a structural transition from a 2D hexagonally packed monolayer to a 3D bcc superlattice assembly. (b) and (c) show higher magnification images of the different structures in (a) and the corresponding unit cells. (d) and (e) illustrate the 2D W–S cells of the bcc (110) plane and the fcc (111) (or hexagonally packed monolayer) plane. The 2D W–S cell for a hexagonally packed cell is more geometrically symmetric than the 2D W–S cell for the bcc (110) plane, which minimizes the energetically unfavorable stretching and compression of organic ligand shells.

hand, twinning in bcc crystals occurs on {112} planes (and not {110} planes), which are oriented perpendicular to the substrate and clearly visible by TEM.

In summary, bcc superlattices of 1.8 nm dodecanethiol-capped Au nanocrystals, 3.7 nm oleic acid-capped PbS nanocrystals, and 7.9 nm oleic acid-capped PbSe nanocrystals were studied by TEM and GISAXS. By considering the Wigner-Seitz cells of the bcc and fcc superlattices, we show that ligand packing frustration always favors bcc structure, especially when ligand interpenetration can occur. When the nanocrystal cores are relatively small and the interparticle attractions are much less than  $0.1 kT$  or so, the entropic penalty due to ligand packing frustration becomes significant. This is the reason that small dodecanethiol-capped Au nanocrystals with less than 2 nm diameter always form bcc superlattices for example.<sup>14,22</sup> Ligand packing entropy also favors hexagonal monolayers, which explains the fact that non close-packed monolayers of nanocrystals are rarely observed.<sup>13</sup> It is also worth noting that chain packing entropy is a critical consideration in understanding the phase behavior of amphiphilic diblock copolymers, as early theories that did not consider it could predict bcc formation and even hexagonal monolayers,<sup>47</sup> but failed to predict other phases.<sup>34,46</sup> The bcc nanocrystal superlattices tend to exhibit a significant amount of {112} twinning after drying on a substrate. These twin planes can form in response to the lateral shear forces occurring during the evaporation of the solvent. The crystallographic orientations of fcc and bcc superlattices and their twin planes with respect to the

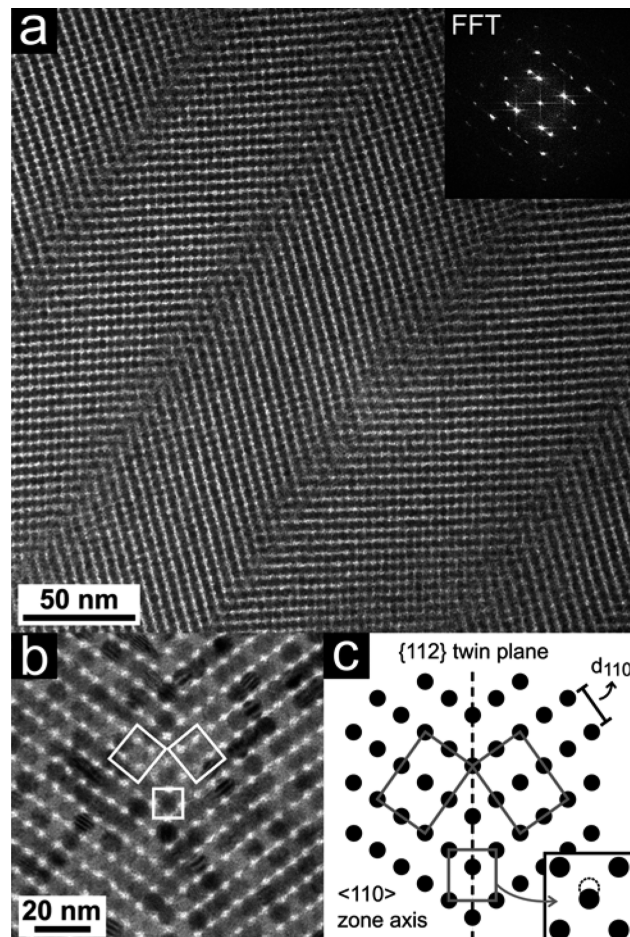


**Figure 6.** (a) TEM image and corresponding FTT of parallel {112} twin planes imaged down a {110} zone axis of a bcc superlattice of 3.7 nm diameter PbS nanocrystals. A detailed view of a single twin plane in a bcc superlattice of 7.9 nm diameter PbSe nanocrystals is shown in (b) and represented schematically in (c). The upper two rectangles show two bcc unit cells reflected across the twin plane, and the lower rectangle highlights that the positions of the atoms along the twin plane are shifted slightly along the {111} direction.

deposition substrate are different, favoring the formation and observation of superlattice twins in bcc assemblies.

## ■ ASSOCIATED CONTENT

### S Supporting Information

Detailed descriptions of experimental methods, calculation of the distribution of ligand lengths in bcc and fcc superlattices, nanocrystal core size measurements by solution SAXS, and additional TEM images of monolayer-to-multilayer structural transitions and bcc superlattice twinning. The Supporting Information is available free of charge on the ACS Publications website at DOI: 10.1021/acs.jpclett.5b00946.

## ■ AUTHOR INFORMATION

### Corresponding Author

\*E-mail: korgel@che.utexas.edu; (T) (512) 471-5633; (F) (512) 471-7060.

### Notes

The authors declare no competing financial interest.

## ACKNOWLEDGMENTS

We thank Michael Rasch and Matthew Panthani for synthesizing nanocrystals and Colin Hessel and Julián Villarreal for assistance in collecting SAXS data. This work was supported in part by funding from the Robert A. Welch Foundation (Grant no. F-1464) and the National Science Foundation (Grant no. CBET-140378). CHESS is supported by the NSF & NIH/NIGMS via NSF awards DMR-0936384 and DMR-1332208. B.W.G. acknowledges financial support under the NSF IGERT program DGE-0549417.

## REFERENCES

- (1) Alder, B. J.; Wainwright, T. E. Phase Transition for a Hard Sphere System. *J. Chem. Phys.* **1957**, *27*, 1208–1208.
- (2) Pusey, P. N.; van Megen, W.; Bartlett, P.; Ackerson, B. J.; Rarity, J. G.; Underwood, S. M. Structure of Crystals of Hard Colloidal Spheres. *Phys. Rev. Lett.* **1989**, *63*, 2753–2753.
- (3) Eldridge, M. D.; Madden, P. A.; Frenkel, D. Entropy-Driven Formation of a Superlattice in a Hard-Sphere Binary Mixture. *Nature* **1993**, *365*, 35–37.
- (4) Gelbart, W. M.; Ben-Shaul, A. The “New” Science of Complex Fluids. *J. Phys. Chem.* **1996**, *100*, 13169–13189.
- (5) Murray, C. B.; Kagan, C. R.; Bawendi, M. G. Self-Organization of CdSe Nanocrystallites into Three-Dimensional Quantum Dot Superlattices. *Science* **1995**, *270*, 1335–1338.
- (6) Korgel, B. A.; Fullam, S.; Connolly, S.; Fitzmaurice, D. Assembly and Self-Organization of Silver Nanocrystal Superlattices: Ordered “Soft Spheres”. *J. Phys. Chem. B* **1998**, *102*, 8379–8388.
- (7) Sigman, M. B.; Saunders, A. E.; Korgel, B. A. Metal Nanocrystal Superlattice Nucleation and Growth. *Langmuir* **2004**, *20*, 978–983.
- (8) Constantinides, M. G.; Jaeger, H. M.; Li, X.; Wang, J.; Lin, X.-M. The Formation and Characterization of Three-Dimensional Gold Nanocrystal Superlattices. *Z. Kristallogr.* **2007**, *222*, 595–600.
- (9) Tam, E.; Podsiadlo, P.; Shevchenko, E.; Ogletree, D. F.; Delplancke-Ogletree, M.-P.; Ashby, P. D. Mechanical Properties of Face-Centered Cubic Supercrystals of Nanocrystals. *Nano Lett.* **2010**, *10*, 2363–2367.
- (10) Saunders, A. E.; Sigman, M. B.; Korgel, B. A. Growth Kinetics and Metastability of Monodisperse Tetraoctylammonium Bromide Capped Gold Nanocrystals. *J. Phys. Chem. B* **2004**, *108*, 193–199.
- (11) Korgel, B. A.; Fitzmaurice, D. Small-Angle X-Ray-Scattering Study of Silver-Nanocrystal Disorder-Order Phase Transitions. *Phys. Rev. B* **1999**, *59*, 14191–14191.
- (12) Whetten, R. L.; Shafiqullin, M. N.; Khouri, J. T.; Schaaff, T. G.; Vezmar, I.; Alvarez, M. M.; Wilkinson, A. Crystal Structures of Molecular Gold Nanocrystal Arrays. *Acc. Chem. Res.* **1999**, *32*, 397–406.
- (13) Goodfellow, B. W.; Patel, R. N.; Panthani, M. G.; Smilgies, D.-M.; Korgel, B. A. Melting and Sintering of a Body-Centered Cubic Superlattice of PbSe Nanocrystals Followed by Small Angle X-ray Scattering. *J. Phys. Chem. C* **2011**, *115*, 6397–6404.
- (14) Goodfellow, B. W.; Rasch, M. R.; Hessel, C. M.; Patel, R. N.; Smilgies, D.-M.; Korgel, B. A. Ordered Structure Rearrangements in Heated Gold Nanocrystal Superlattices. *Nano Lett.* **2013**, *13*, 5710–5714.
- (15) Choi, J. J.; Bealing, C. R.; Bian, K.; Hughes, K. J.; Zhang, W.; Smilgies, D.-M.; Hennig, R. G.; Engstrom, J. R.; Hanrath, T. Controlling Nanocrystal Superlattice Symmetry and Shape-Anisotropic Interactions through Variable Ligand Surface Coverage. *J. Am. Chem. Soc.* **2011**, *133*, 3131–3138.
- (16) Bian, K.; Choi, J. J.; Kaushik, A.; Clancy, P.; Smilgies, D.-M.; Hanrath, T. Shape-Anisotropy Driven Symmetry Transformations in Nanocrystal Superlattice Polymorphs. *ACS Nano* **2011**, *5*, 2815–2823.
- (17) Nagaoka, Y.; Chen, O.; Wang, Z.; Cao, Y. C. Structural Control of Nanocrystal Superlattices Using Organic Guest Molecules. *J. Am. Chem. Soc.* **2012**, *134*, 2868–2871.
- (18) Bian, K.; Wang, Z.; Hanrath, T. Comparing the Structural Stability of PbS Nanocrystals Assembled in fcc and bcc Superlattice Allotropes. *J. Am. Chem. Soc.* **2012**, *134*, 10787–10790.
- (19) Henry, A. I.; Courty, A.; Pileni, M. P.; Albouy, P. A.; Israelachvili, J. Tuning of Solid Phase in Supracrystals Made of Silver Nanocrystals. *Nano Lett.* **2008**, *8*, 2000–2005.
- (20) Whetten, R. L.; Khouri, J. T.; Alvarez, M. M.; Murthy, S.; Vezmar, I.; Wang, Z. L.; Stephens, P. W.; Cleveland, C. L.; Luedtke, W. D.; Landman, U. Nanocrystal Gold Molecules. *Adv. Mater.* **1996**, *8*, 428–433.
- (21) Yamamoto, S.; Farrell, D. F.; Majetich, S. A. Direct Imaging of Self-Assembled Magnetic Nanoparticle Arrays: Phase Stability and Magnetic Effects on Morphology. *Phys. Rev. B* **2002**, *65*, 224431.
- (22) Yu, Y.; Jain, A.; Guillaudier, A.; Reddy Voggu, V.; Truskett, T. M.; Smilgies, D.-M.; Korgel, B. A. Nanocrystal Superlattices that Exhibit Improved Order on Heating: an Example of Inverse Melting? *Faraday Discuss.* **2015**, DOI: 10.1039/C5FD00006H.
- (23) Pileni, M. P. Supracrystals of Inorganic Nanocrystals: An Open Challenge for New Physical Properties. *Acc. Chem. Res.* **2008**, *41*, 1799–1809.
- (24) Courty, A. Silver Nanocrystals: Self-Organization and Collective Properties. *J. Phys. Chem. C* **2010**, *114*, 3719–3731.
- (25) Wang, Z.; Schliehe, C.; Bian, K.; Dale, D.; Bassett, W. A.; Hanrath, T.; Klinke, C.; Weller, H. Correlating Superlattice Polymorphs to Internanoparticle Distance, Packing Density, and Surface Lattice in Assemblies of PbS Nanoparticles. *Nano Lett.* **2013**, *13*, 1303–1311.
- (26) Kremer, K.; Robbins, M. O.; Grest, G. S. Phase Diagram of Yukawa Systems: Model for Charge-Stabilized Colloids. *Phys. Rev. Lett.* **1986**, *57*, 2694–2694.
- (27) McConnell, G. A.; Gast, A. P. Predicting Disorder-Order Phase Transitions in Polymeric Micelles. *Phys. Rev. E* **1996**, *54*, 5447.
- (28) Lodge, T. P.; Bang, J.; Li, Z.; Hillmyer, M. A.; Talmon, Y. Strategies for Controlling Intra- and Intermicellar Packing in Block Copolymer Solutions: Illustrating the Flexibility of the Self-Assembly Toolbox. *Faraday Discuss.* **2005**, *128*, 1–12.
- (29) Lodge, T. P.; Bang, J.; Park, M. J.; Char, K. Origin of the Thermoreversible fcc–bcc Transition in Block Copolymer Solutions. *Phys. Rev. Lett.* **2004**, *92*, 145501.
- (30) Luedtke, W. D.; Landman, U. Structure, Dynamics, and Thermodynamics of Passivated Gold Nanocrystallites and Their Assemblies. *J. Phys. Chem.* **1996**, *100*, 13323–13329.
- (31) Landman, U.; Luedtke, W. D. Small is Different: Energetic, Structural, Thermal, and Mechanical Properties of Passivated Nano-cluster Assemblies. *Faraday Discuss.* **2004**, *125*, 1–22.
- (32) Goodfellow, B. W.; Korgel, B. A. Reversible Solvent Vapor-Mediated Phase Changes in Nanocrystal Superlattices. *ACS Nano* **2011**, *5*, 2419–2424.
- (33) Bates, F. S.; Cohen, R. E.; Berney, C. V. Small-angle Neutron Scattering Determination of Macrolattice Structure in a Polystyrene-Polybutadiene Diblock Copolymer. *Macromolecules* **1982**, *15*, 589–592.
- (34) Matsen, M. W.; Bates, F. S. Testing the Strong-Stretching Assumption in a Block Copolymer Microstructure. *Macromolecules* **1995**, *28*, 8884–8886.
- (35) Thomas, E. L.; Kinning, D. J.; Alward, D. B.; Henkee, C. S. Ordered Packing Arrangements of Spherical Micelles of Diblock Copolymers in Two and Three Dimensions. *Macromolecules* **1987**, *20*, 2934–2939.
- (36) Matsen, M. W. The Standard Gaussian Model for Block Copolymer Melts. *J. Phys.: Condens. Matter* **2002**, *14*, R21–R47.
- (37) Gruner, S. M. Stability of Lyotropic Phases with Curved Interfaces. *J. Phys. Chem.* **1989**, *93*, 7562–7570.
- (38) Kramer, E. J. Phase Transitions in Thin Block Copolymer Films. *MRS Bull.* **2010**, *35*, 457–465.
- (39) Saunders, A. E.; Korgel, B. A. Second Virial Coefficient Measurements of Dilute Gold Nanocrystal Dispersions Using Small Angle X-ray Scattering. *J. Phys. Chem. B* **2004**, *108*, 16732–16738.

- (40) Shah, P. S.; Holmes, J. D.; Johnston, K. P.; Korgel, B. A. Size-Selective Dispersion of Dodecanethiol-Coated Nanocrystals in Liquid and Supercritical Ethane by Density Tuning. *J. Phys. Chem. B* **2002**, *106*, 2545–2551.
- (41) Smilgies, D.-M.; Heitsch, A. T.; Korgel, B. A. Stacking of Hexagonal Nanocrystal Layers during Langmuir–Blodgett Deposition. *J. Phys. Chem. B* **2012**, *116*, 6017–6026.
- (42) Heath, J. R.; Knobler, C. M.; Leff, D. V. Pressure/Temperature Phase Diagrams and Superlattices of Organically Functionalized Metal Nanocrystal Monolayers: The Influence of Particle Size, Size Distribution, and Surface Passivant. *J. Phys. Chem. B* **1997**, *101*, 189–197.
- (43) Ye, X.; Chen, J.; Murray, C. B. Polymorphism in Self-Assembled AB<sub>6</sub> Binary Nanocrystal Superlattices. *J. Am. Chem. Soc.* **2011**, *133*, 2613–2620.
- (44) McConnell, G. A.; Lin, M. Y.; Gast, A. P. Long Range Order in Polymeric Micelles under Steady Shear. *Macromolecules* **1995**, *28* (20), 6754–6764.
- (45) Ackerson, B. J.; Clark, N. A. Shear-Induced Partial Translational Ordering of a Colloidal Solid. *Phys. Rev. A* **1984**, *30*, 906–906.
- (46) Rupich, S. M.; Shevchenko, E. V.; Bodnarchuk, M. I.; Lee, B.; Talapin, D. V. Size-Dependent Multiple Twinning in Nanocrystal Superlattices. *J. Am. Chem. Soc.* **2010**, *132*, 289–296.
- (47) Leibler, L. Theory of Microphase Separation in Block Copolymers. *Macromolecules* **1980**, *13*, 1602–1617.